Impact of thermal annealing on magnetic properties in nanostructured compositionally complex spinel cobaltite - $(Mg_{0.2}Mn_{0.2}Fe_{0.2}Cu_{0.2}Zn_{0.2})Co_2O_4$

Xin Wang,* Cameron Sparks Jorgensen, Corisa Kons, Peter C. Metz,
Joshua Safin, William Meier, Dustin A. Gilbert, and Katharine Page†
Department of Materials Science and Engineering, Institute for Advanced Materials and Manufacturing, University of Tennessee, Knoxville, Tennessee 37996 United States

Yuanpeng Zhang and Jue Liu
Neutron Scattering Division, Oak Ridge National Laboratory, Oak Ridge, Tennessee 37831 United States

Eleonora Calì
Department of Applied Science and Technology, Politecnico di Torino, Turin 10129 Italy
(*kpage10@utk.edu)
(Dated: September 24, 2025)

Exploring the controllable aspects of local atomic structure and chemical ordering and their correlations with functional properties is crucial for harnessing the potential of complex oxides in the development of advanced materials. In this work, we have investigated the sensitivity of the magnetic properties in a nanostructured metastable spinel compositionally complex oxide (CCO) composition, $(Mg_{0.2}Mn_{0.2}Fe_{0.2}Cu_{0.2}Zn_{0.2})Co_2O_4$, to local chemical segregation and phase evolution introduced through variation in post-processing heat treatment temperature. A combination of X-ray diffraction, scanning transmission electron microscopy with energy dispersive X-ray spectroscopy (STEM-EDS), first-order reversal curve (FORC) magnetometry, and neutron diffraction and total scattering analyses was employed to understand both average and local structure-property evolution. Structure analysis shows that the post-annealing process triggers local and long-range cation diffusion, resulting in changes in the distribution of atoms residing on the tetrahedral and octahedral sites of the spinel structure as well as nanoscale chemical heterogeneity. FORC analysis shows that redistribution of magnetic cations induces subtle magnetic phase separation and soft to hard magnetic phase transformations, and demonstrates incipient demixing of the as-synthesized material well before detection by neutron total scattering. This work additionally highlights the necessity of a combination of advanced characterization techniques for understanding the broader crystal-chemical class of compositionally complex oxides.

I. INTRODUCTION

Limited research has been conducted on the impact of processing parameters on nanostructured high entropy oxides (HEOs) or compositionally complex oxides (CCOs). It is widely acknowledged in the scientific community that complex oxides can exhibit a notable degree of chemical short-range order (CSRO), distinct nanoscale phase segregation, and local lattice distortion. Moreover, specific local atomic ordering patterns and their coherent length scales are often tied to distinct physical properties[1–4]. For example, disorder amongst Ni and Mn sites affects the surface and near-surface properties to control electrochemical performance of $LiNi_{0.44}Mn_{1.56}O_4$ lithium-ion batteries (LIBs)[5], local compositional disorder generates tunable magnetic properties in single crystal $La(Cr_{0.2}Mn_{0.2}Fe_{0.2}Co_{0.2}Ni_{0.2})O_3$ films[6], and the ratio of Co^{3+}/Co^{2+} and M^{3+}/M^{2+} on the octahedral site determines the oxygen evolution reaction (OER) activity of MCo_2O_4 (M = Mn, Fe, Co, Ni, and Zn) spinels[7]. Other complex oxides are imbued with unique properties via nanoscale phase segregation, including relaxor ferroelectrics[8, 9], birefringent garnets[10], spinel and rock salt exchange spring magnets[11] and electrochemical cycling platforms[12]. Others feature coherent architectures with fine compositional gradients that enable distinct physicochemical properties[13, 14]. Clearly, design paradigms for control of chemical and phase segregation and coupling at the atomic and nano scales are of broad interest. Following this reasoning, the extraordinary complexity found in HEOs and CCOs is hypothesized to present rich opportunities for harnessing complex diffusion dynamics through tailored synthesis approaches to stabilize novel local atomic configurations and defects, enabling rational design of highly performant materials[15–17].

From the perspective of magnetic behavior, particularly in oxides, CCO properties will depend on the elements present, their valence states, and their specific coordination environments within the structure. Among the 3d transition metals, cobalt-containing advanced magnetic materials exhibit high saturation magnetization (M_S) and high Curie temperature (T_C)[18]. The end member cobaltites ACo_2O_4 (A=Mg, Mn, Fe, Ni, Cu, Zn, Co) are earth-abundant ferrimagnets that crystallize in the spinel structure[19–25]. In the normal spinel structure (Figure 1 (a)), large divalent cations occupy the tetrahedral A-site exclusively, while trivalent Co occupies the octahedral B-site. Figure 1 (b) displays the corresponding ferrimagnetic structure with calculated magnetic moments on tetrahedral and octahedral cation sites aligned in opposite directions along the c-axis. Commonly, there is

* Current address: Chemical Sciences Division, Oak Ridge National Laboratory, Oak Ridge, Tennessee 37831 United States
† Neutron Scattering Division, Oak Ridge National Laboratory, Oak Ridge, Tennessee 37831 United States

some cation mixing between the A- and B- sites; the fraction of A-site cations occupying the B-site, called the inversion parameter (γ), ranges from 0 for normal spinel to 1 for inverse spinel, and the degree of inversion influences the ferrimagnetism[26]. Additionally, the magnetic properties of spinels, including the blocking temperature, saturation magnetization, remnant magnetization, and coercivity, are known to be influenced by factors such as nanocrystalline shape[27] and compositional tuning[28, 29]. Compositionally complex cobaltites expand upon this design space considerably, as the local and long-range nuclear and spin structures will depend on a large number of metal-oxygen-metal couples due to the many cation types, varying coordination geometries, valence and spin states HEOs and CCOs possess[26].

In the high-entropy paradigm, configurational entropy (S_{config}) may stabilize otherwise unfavorable structures; yet, in the spinel system, the configurational entropy is found to be consistently smaller than the threshold for classification as HEO (1.5 R, where R is the universal gas constant), even when the number of distinct cations on the A site reaches 8[30]. The category CCO is more appropriate in this case as it encompasses medium-entropy and non-equimolar composition oxides[31]. Our previous study of CCO cobaltites synthesized by a low-temperature soft-templating (LTST) method revealed that the phase selectivity and temperature stability are primarily influenced by the chemical composition rather than the number of participating cations and that these cobaltites are metastable rather than entropy stabilized[16]. Additionally, our investigation of their electrocatalytic properties highlighted that the bifunctional oxygen evolution reaction (OER) and oxygen reduction reaction (ORR) is significantly influenced by cation combination and post-annealing temperatures[32]. Thus, it becomes apparent that the synthesis conditions play an essential role in determining the metastable state of the sample and in the resulting material behavior[30]. Consequently, this family of compounds provides a versatile phase space where competing thermodynamic factors and sluggish cation diffusion can be exploited to tailor cation site inversion, the heterogeneity of the cation distribution over different length scales, and the resulting material properties.

To accelerate the development of HEO and CCO complex functional oxides, it is crucial to understand to what extent their local environments can be controlled and linked to functional properties. In this paper, we investigate the sensitivity of magnetic properties to the thermal history of the nanostructured compositionally complex spinel $(Mg_{0.2}Mn_{0.2}Fe_{0.2}Cu_{0.2}Zn_{0.2})Co_2O_4$. High-resolution scanning transmission electron microscopy (STEM), first-order reversal curve (FORC) measurements from bulk magnetometry, and average and local atomic structure analysis from neutron total scattering experiments are combined to reveal trends in structure-property relationships. By controlling post-annealing temperatures (600°C, 800°C, and 1000°C) and hence the degree of cation diffusion in the system, the chemical short-range order, cation site preference, phase segregation, and the morphology of nanostructures can be tuned. The resulting specific local ordering patterns lead to distinct magnetic behaviors, highlighting the potential of nanostructured HEO and CCO materials as highly tunable platforms for magnetic applications.

II. METHODS

A. Materials synthesis

CCOs with the composition, $(Mg_{0.2}Mn_{0.2}Fe_{0.2}Cu_{0.2}Zn_{0.2})Co_2O_4$ were synthesized using a low-temperature soft templating (LTST) reaction method, the details of which were previously published[16]. The gel obtained from the evaporation of room temperature solution was initially calcined at 400°C, leading to the formation of the as-formed sample in this work. Subsequently, all post-annealing treatments were conducted on pellets made from this same as-formed 'precursor' sample, separately, at temperatures of 600°C, 800°C, and 1000°C.

B. Characterization

1. X-ray diffraction (XRD)

XRD measurements were conducted on all four samples using Co Kα radiation with a PANalytical Empyrean diffractometer. The XRD patterns were collected from 10 to 90° 2θ with a step size of 0.026°. The specimen was prepared by placing a small amount of finely ground powder onto a 0.2 mm deep well of the zero background silicon sample holder, after which a glass slide was used to compress a flat surface for measurements.

2. Electron microscopy

The sample morphology at the nanoscale was examined by scanning transmission electron microscopy (STEM) using a JEOL JEM-2100F microscope. The incident beam was operated at 200 kV. To determine the chemical composition and elemental distribution, energy dispersive X-ray spectroscopy (EDS) (80 mm X-Max detector, Oxford Instruments) was employed. To prepare the STEM-EDS specimen, the powder samples were sonicated in high-purity propan-2-ol and then drop-cast on copper grids coated with a holey carbon film (3.05 mm diam. 300 mesh, TAAB Laboratories Equipment Ltd).

To quantitatively analyze the trend of chemical homogeneity observed in the STEM-EDS images, a statistical analysis was conducted based on the pixel intensities within the elemental colormaps. A dataset containing each element's intensity was constructed on a per pixel basis, and the frequency of the intensities of each element was determined. First, the resulting shape of the distributions was evaluated to determine if the elements are randomly distributed (by checking for skewness, modality, or narrowing of the distribution that would

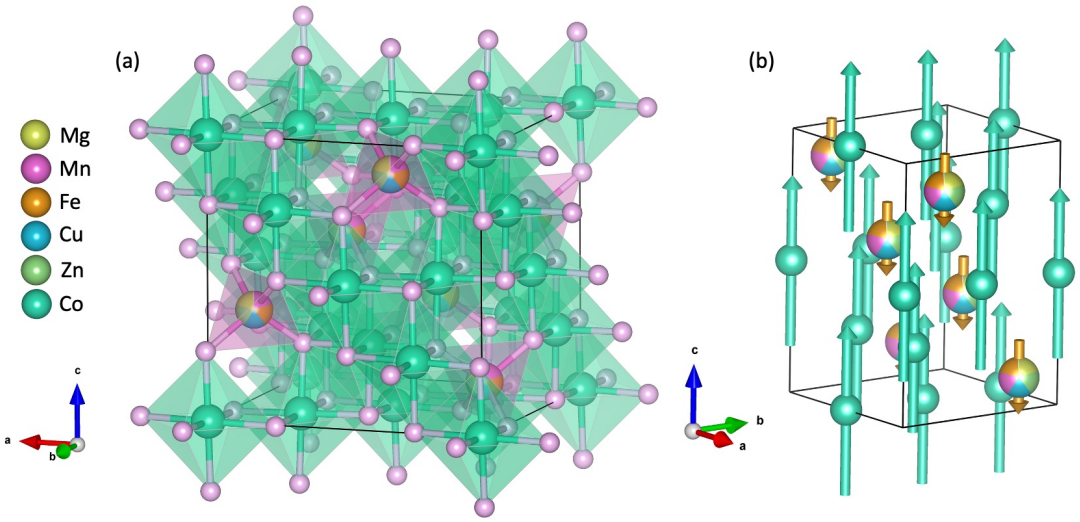

FIG. 1. (a) Normal spinel unit cell comprises pink tetrahedra (A-sites) and green octahedra (Co-sites), with atoms labeled in their respective colors. The A-site cations, including Mg, Mn, Fe, Cu, and Zn occupy the tetrahedral site, while Co occupies only the octahedral site. (b) The corresponding room-temperature zero-field magnetic spinel structure depicts calculated magnetic moments pointing down on the tetrahedral site and pointing up on the octahedral site. Oxygen atoms have been removed from (b) for clarity.

suggest correlations with other elements and departure from a normal distribution). Secondly, for each elemental pair, correlation coefficients were calculated, giving quantitative values for the relationships among element ordering[33, 34]. If all elements are weakly correlated, the composition is at a near stoichiometric ratio at each location within the sample. Strong positive correlations are representative of clustering; when one element is in high concentration in a pixel, the correlated element is also in high concentration. Strong negative correlations are representative of segregation. A spot with a high concentration of one element will have a low concentration of the negatively correlated element and vice versa. All together analysis of the distribution and correlation helps to give a greater understanding of the ordering than just the color images alone.

C. Magnetic measurements

The magnetometry measurements on all samples were carried out using a vibrating sample magnetometer (VSM) as part of a Quantum Design PPMS DynaCool system. With 100 Oe field applied, the magnetization was measured as the temperature was decreased from 300 K to 2 K to obtain the FC curve. The quantified interactions[35] and reversal mechanisms[36] were investigated using the first-order reversal curve (FORC) technique[35, 37–39]. The protocol of FORC measurements starts with first applying a large positive field to saturate the sample, then the field is gradually reduced to a specific reversal field (H_R), and then the magnetization is measured as the applied field (H) is increased from H_R to saturation. This process was repeated to obtain a family of FORCs at H_R between negative and positive saturation. The FORC distribution, ρ (H, H_R) is defined as applying a mixed second-order derivative to the dataset

$$\rho(H,H_R) = \frac{-1}{2M_S}\frac{\partial^2 M(H,H_R)}{\partial H \partial H_R} \tag{1}$$

where M_S is the magnetization saturation. In effect, the derivative $\partial M/\partial H$ of each FORC branch is compared to its adjacent neighbors, capturing any new or moving magnetic switching events. Measurements conducted with increasing magnetic field, e.g. the H axis, are probing magnetic up-switching events from a negative to a positive orientation, while H_R probes down-switching events. FORC measurements were conducted to examine all four samples processed at various temperatures, focusing on the small bump observed at low temperatures in M vs T plots for each sample. The specific temperatures 5 K and 100 K were applied to all four samples. The resulting FORC diagram represents a contour plot of ρ (H, H_R). Associating H with up-switching events and H_R with down-switching, the data is transformed into a new coordinate system representing the local coercivity and bias: $H_C = (H - H_R)/2$ and $H_B = (H + H_R)/2$.

Finally, magnetic hysteresis (M_H) loop measurements at 5 K and 100 K were extracted from the family of FORCs for all the samples. All measurements were normalized to the sample mass.

D. Neutron total scattering measurements

Time of flight (TOF) neutron powder diffraction (NPD) data and neutron total scattering data were collected on the Nanoscale Ordered Materials Diffractometer (NOMAD) at the Spallation Neutron Source (SNS) at Oak Ridge National Laboratory (ORNL)[40]. For each sample, approximately 0.3 g of powder was dried at 200 °C for two days and loaded

into a 3 mm diameter quartz capillary. Data collection for all four samples was performed at 300 K in a temperature-controlled Ar cryostream. Data reduction, including normalization, background subtraction, and absorption correction, was carried out using the MantidTotalScattering (MTS) framework. Pair distribution function (PDF) data was Fourier transformed from total scattering data using a Q_{max} of 32 Å^{-1}.

E. Rietveld and PDF refinement

Rietveld refinements were carried out with the TOPAS-V7 program[41]. For the main spinel phase structure (space group $Fd\bar{3}m$), the background, scale factors, lattice parameters (a), A-, B-, and O-site isotropic atomic displacement parameters (B_{iso}), and oxygen atom positions were refined. Only lattice parameters and scale factors were refined for the impurities present in samples that were post-annealed at 800°C and 1000°C. It was found necessary to employ a two-spinel phase to fit the 1000°C data. A lattice parameter and phase fraction were refined for the secondary spinel phase. The atomic displacement parameters in the secondary spinel phase were constrained as equal to those in the main spinel phase. To address the intricate nature of the cation site mixing in this nano CCO and avoid over-fitting, the A- and B- sites of spinel phases were treated as pseudo-atoms; only the average scattering length on each site was refined. Finally, isotropic crystallite size and microstrain broadening were applied to describe the nanomaterial peak broadening in the phases[42, 43].

Ferrimagnetic order in nano spinel CCO structures is potentially detectable via magnetic scattering. However, magnetic contributions to the neutron diffraction intensities were found negligible for all samples and were excluded in the final fits. This observation is consistent with Figure 4, where the very low mass magnetization (~ 0.01 μ_B/F.U.) at 300 K likely falls below the sensitivity threshold for magnetic structure neutron diffraction detection. Due to the substantial net cancellation of magnetic moments inherent to ferrimagnetic structures, diffuse locally correlated magnetic moments of the nano-CCOs cannot be explicitly ruled out based on the data collected and may warrant further investigation.

Structure refinements against PDF data were also performed using TOPAS-V7[41], utilizing both a single-phase spinel model (1-phase) and the two-spinel phase (2-phase) model described above for all sample data. The 2-phase model was found to more accurately capture the low r peak shapes across the data series, with significantly improved goodness of fit R_{wp} values and smaller atomic displacement parameters (B_{iso}, Å^2) compared to the single spinel model. The PDF refinements conducted with 30 Å range using both the 1-phase and 2-phase models are illustrated in Figure 8. By incorporating the secondary spinel phase, only the lattice parameter (a), scale factor, and the average scattering lengths ($\langle b \rangle$, fm) for both tetrahedral and octahedral sites are refined. The corresponding extracted phase percentages (p, %), lattice parameters (a, Å), average scattering lengths ($\langle b \rangle$, fm), and the atomic displacement parameters of tetrahedral cation, octahedral cation, and oxygen atom sites (B_{iso}, Å^2) are compared in Figure S1. The minor influence of magnetic scattering was ignored in PDF modeling, based on the small intensity of magnetic scattering observed via Rietveld refinement at 300 K. However, it was found necessary to include the impurity phase, MgO, to achieve satisfactory PDF fits for the sample post-annealed at 1000°C. Instrument resolution effects were modeled using parameters determined through the refinement of a nickel powder data set.

III. RESULTS AND DISCUSSION

A. Phase purity and nanoscale heterogeneity

The post-annealing process induced changes in the phase purity as well as particle size and morphology of samples, as revealed by X-ray powder diffraction (Figure 2(a)) and bright-field STEM analysis (Figure 2(b-e)). The XRD pattern for the sample only calcined at 400°C confirms the expected cubic spinel $Fd\bar{3}m$ structure. However, increasing post-annealing temperature led to the formation of additional phases; the XRD pattern of the sample post-annealed at 600°C reveals a minor impurity peak (near the noise level) at 73° 2θ, which aligns with the prominent rocksalt (MgO) peak observed in the XRD patterns of samples post-annealed at 800°C and 1000°C; the XRD pattern of the sample post-annealed at 800°C reveals the presence of tenorite (CuO) and rocksalt (MgO), and the XRD pattern of the sample post-annealed at 1000°C exhibits CuO and MgO, as well as a secondary spinel phase. Rietveld refinements for samples post-annealed at 800°C and 1000°C are shown in the SI Figure S2. Further insight can be gained by considering changes in the diffraction peak shapes of the samples. Broad and asymmetric peaks were observed within the samples calcined at 400°C and post-annealed at 600°C, suggesting the possible existence of multiple different nanostructured regions rather than a true solid solution[16]. The trend towards sharper, more symmetric peaks in the post-annealed samples indicates equilibration towards greater chemical homogeneity as well as increased crystallite size.

These microstructure characteristics are further supported by the STEM images shown in Figure 2 (b-e), where the samples calcined at 400°C and post-annealed at 600°C exhibit a larger particle size distribution compared to the other two post-annealed samples. Further, the distribution of elements among representative particles or domains in the samples was examined via STEM-EDS elemental mapping (Figure 3). It can be seen, by comparing the maps for samples (a) calcined at 400°C, (b) post-annealed at 600°C, (c) post-annealed at 800°C and (d) post-annealed at 1000°C, that post-annealing induces a redistribution of cations among particles and grains. In the as-formed 400°C condition, Mg, Mn, and Fe are enriched in specific domains, with a similar but less pronounced inhomogeneous distribution for Zn (Figure 3(a)). In samples post-annealed at 600°C (Figure 3(b)) and 800°C (Figure 3(c)) the cation distributions appear slightly more homogeneous, though certain grains maintain enrichment of select elements. In the sample post-annealed at 800°C (Figure 3(c)) MgO pre-

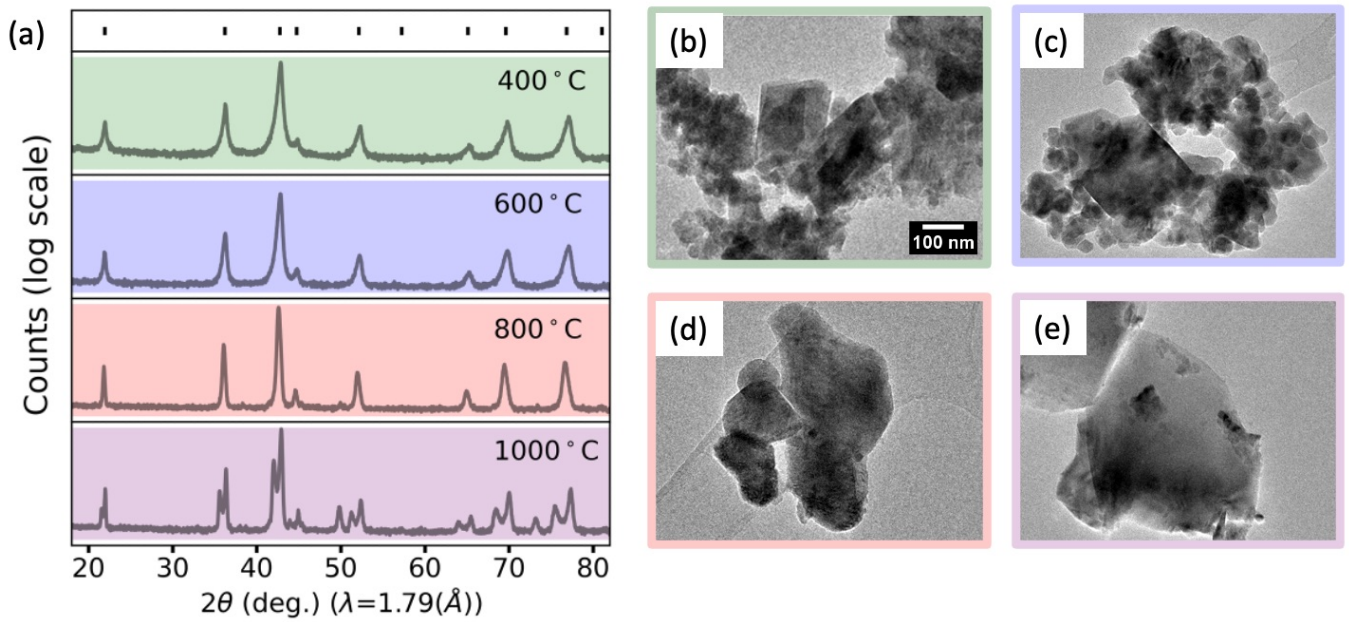

FIG. 2. (a) XRD pattern comparison of samples indicating a single spinel phase for 400°C and 600°C samples and impurity/secondary phases for 800°C and 1000°C samples. The small black solid (h k l) ticks placed in the bar on top of the XRD patterns indicate Bragg peak locations of the main spinel phase. (b-e) STEM image comparison of samples (b) calcined at 400°C, and post-annealed at (c) 600°C, (d) 800°C, and (e) 1000°C. The samples calcined at 400°C and post-annealed at 600°C display broad particle size distributions. In contrast, the sample post-annealed at 800°C exhibits particle sizes of 100 nm or more. The sample post-annealed at 1000°C consists of micron-scale sized particles. Note the same scale bar applies to all four STEM images in (b-e).

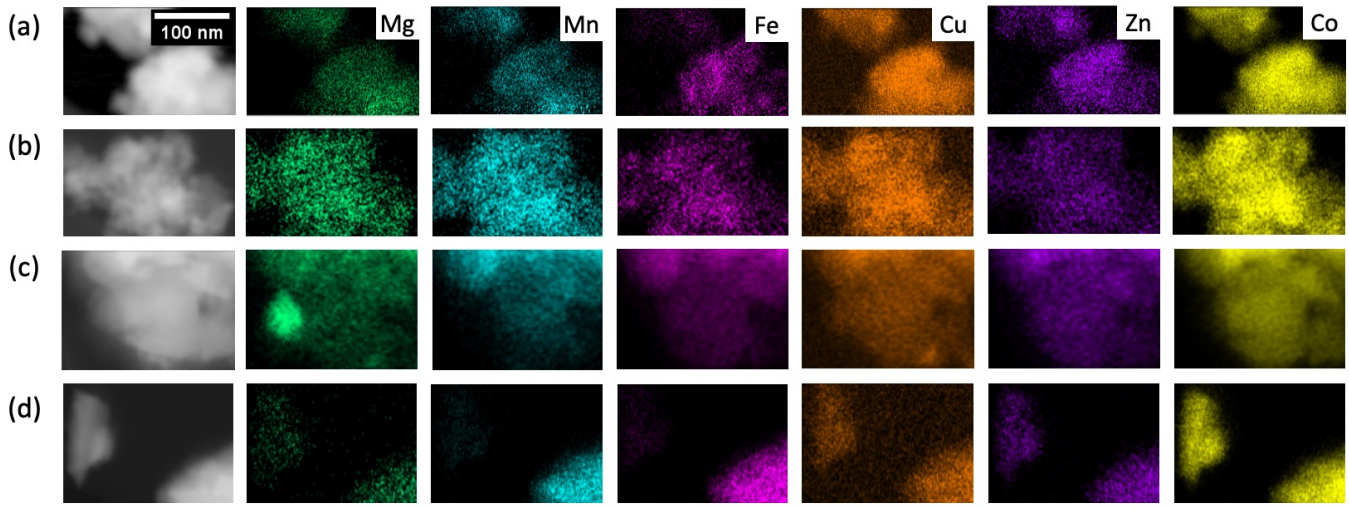

FIG. 3. STEM-EDS map of $(Mg_{0.2}Mn_{0.2}Fe_{0.2}Cu_{0.2}Zn_{0.2})Co_2O_4$ spinel (a) as prepared at 400°C, and after post-annealing heat treatment at (b) 600°C, (c) 800°C, and (d) 1000°C. Note the first column of images on the left are STEM high-angle annular dark-field (HAADF) images. The scale bar in the top left corner applies to all images.

cipitation was identified, in agreement with XRD analysis. It should be noted that the phase fraction of the CuO impurity refined by Rietveld analysis is less than 2 wt%, making it challenging to observe via the STEM-EDS technique. Lastly, for the sample post-annealed at 1000°C (Figure 3(d)), both the precipitation of MgO and a deficiency of Mn and Fe in a sizable fraction of particles are apparent.

In summary, intermediate post-annealing temperatures are seen to induce cation diffusion. At higher post-annealing temperatures, cation diffusion induced rock salt and tenorite impurities precipitate, even separate spinel phases emerge; one with predominantly Mg, Cu, Zn, and Co, and another necessarily enriched in Fe and Mn. These observations reveal a complex phase evolution occurring over multiple length-

scales in the CCO spinel. However, determining overall cation diffusion trends proves challenging, even with the statistical analysis of the STEM-EDS mappings. Correlation coefficients, calculated for the relationship of concentrations between individual element pairs (illustrated in Figure S3) and the distribution of frequencies of the concentration of each element, were plotted for each EDS map and can be found in SI Figure S4 and S5 for the sample post-annealed at 400°C, S6 and S7 for the sample post-annealed at 600°C, S8 and S9 for the sample post-annealed at 800°C, and S10 and S11 for the sample post-annealed at 1000°C. From these, we see that the samples are heterogeneous with varying levels of segregation (strong negative correlations), clustering (strong positive correlations), or neither, depending on the element pair. There is also a variety of distribution of the concentrations across the various maps. Importantly, we see that across different regions of a sample at a specific processing condition, there are noticeable differences in the correlations between the elements and the distribution of concentration for each element. Thus, while the homogeneity can potentially be seen to be changing as the processing temperature is varied, a definite trend with the processing temperature cannot be easily determined. The samples remain significantly heterogeneous across processing variations.

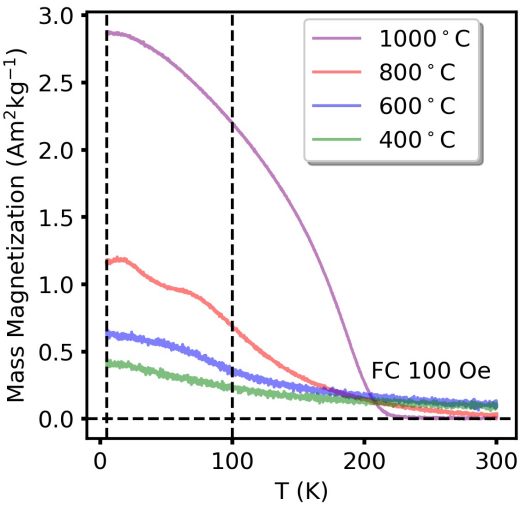

FIG. 4. The field-cooled (FC) comparison for all four samples over a temperature range of 2 K to 400 K with an applied field of 100 Oe. The heat-treatment temperatures are indicated in the legend. The temperatures (5 K and 100 K) used in all FORC measurements are denoted by black dashed vertical lines.

B. Magnetic phase segregation

The results of temperature-dependent magnetometry and magnetic hysteresis measurements for all four samples are shown in Figure 4 and Figure 5, respectively. Overall, the magnetization rises with the increase in post-annealing temperature. For all the samples, increasing the measurement temperature decreases the sample magnetic moment and weakens the ferrimagnetism, as is normally expected. The Curie temperatures, T_Cs, for the samples post-annealed at 1000°C and 800°C are $\approx$ 200 K and $\approx$ 300 K, respectively, while the T_Cs of the samples calcined at 400°C and post-annealed at 600°C are higher than 400 K, beyond the limits of our instrument. In the FC measurements, shown in Figure 4, the sample post-annealed at 800°C exhibits two minor peaks below 100 K, and the sample post-annealed at 600°C exhibits similar but much weaker features (see inset for detail).

The magnetic hysteresis measurements, shown in Figure 5, for all the samples measured at 100 K show a typical hysteresis loop with a coercivity of between 0.5 kOe for the sample calcined at 400°C and 2.2 kOe for the sample treated at 1000°C. Measurement performed at 5 K starts to show a stepped transition, with the reversal of a magnetically soft phase occurring near $H = 0$, followed by a long tail that extends beyond 1 T, corresponding to a magnetically hard phase.

More details about the magnetic structure and reversals can be ascertained from the FORC distributions for all of the samples, measured at 5 K and 100 K, which are shown in Figure 6. The FORC distributions for the sample calcined at 400°C measured at 5 K and 100 K (Figure 6(a) and (b)) are dominated by the same general feature located at $H_C = H_B \approx 0$, corresponding to the soft magnetic phase and showing no coupling to any hard phase. The FORC distribution measured at 100 K (Figure 6(d)) for the sample post-annealed at 600°C shows similar features. By contrast, the FORC distributions measured at 5 K (Figure 6(c)) reveal two distinct features: Feature 1 is predominantly oriented along the H_C axis (local coercive field) and Feature 2 is aligned along the H_B axis (local bias/interaction field), corresponding to the hard and soft phases, respectively. Feature 1 indicates the emergence of a hard phase typically observed in bulk magnets, and in particular in geomagnetism[39]. In contrast, Feature 2 indicates a magnetically soft – likely reversible behavior. Broadening of Feature 2, as well as their mutual proximity in the FORC distribution, suggests that these features are coexistent, and coupled. The soft phase in particular is centered at $H_B = 0$ and is reasonably symmetric along the H_B axis, indicating that it is dominating the reversal behavior, 'dragging' the hard phase with it during reversal. Moving to the sample treated at 800°C, at 100 K, Feature 1 dominates the FORC distribution, centered at $H_C \approx 500$ Oe, although some of Feature 2 persists. The 5 K data also shows a further enhancement of Feature 1 and the features are still coupled. Compared to the sample treated at 600°C, Feature 2 now is notably asymmetric, with a feature extending towards H_B, indicating that Feature 1 is biasing its reversal. This indicates an increase in the magnetic volume of the hard phase and its effective anisotropy. This trend is enhanced in the final sample, which was post-annealed at 1000°C. In both the 5 K and 100 K measurements, Feature 1 dominates the FORC distribution, and the feature representing the soft phase is asymmetric (at 100 K) and fully biased (at 5 K). This indicates that nearly all of the soft phase is coupled to and dominated by an adjacent hard phase. The trends indicate that all of the samples have a mixture of magnetic hard and soft phases, with the hard phase being vanishingly weak

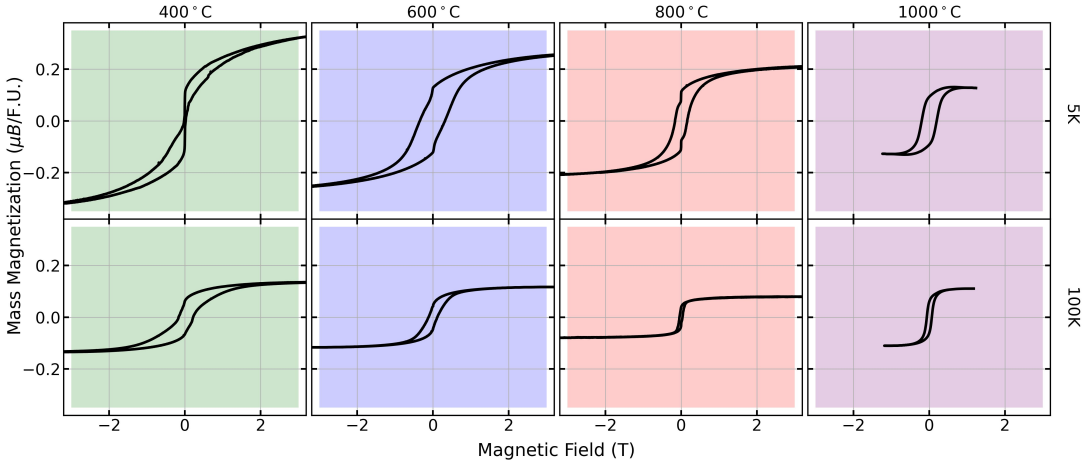

FIG. 5. Magnetometry data for all four samples measured at 5 K (top panels), and 100 K (bottom panels). The heat-treatment temperatures are indicated at the top of each column.

in the samples calcined at 400°C, and increasing to dominate in the samples annealed at 1000°C. The FORCs indicate that these phases are coexistent, with strong magnetic coupling, allowing the soft phase to cause a premature reversal of the hard phase, and later the hard phase to anchor and bias the reversal of the soft phase. Finally, it is notable that the hard feature in particular is a well-established signature of localized reversal – as contrasted with e.g. reversal by domain propagation.This structure indicates that the material is rich in soft nucleation sites which initialize localized structures, and pinning sites, which restrict long-range domain propagation. Combining the FORC measurements with the temperature dependent magnetization, it is likely that the soft phase is transforming into the hard phase, which has a lower T_C, eventually achieving a configuration that is magnetically hard at low temperatures, but non-magnetic at room temperature.

In this specific case, with a large number of cations that can take up positions in two different crystallographic sites and deplete or concentrate in populations within specific particles/grains, it is challenging to determine whether there is a non-magnetic phase and the saturation magnetization of each phase present. This prevents direct determination of the exact structural cation migration from FORC analysis. Regardless, these results complement nanoscale STEM-EDS analysis which indicates thermally activated cation diffusion leads to different heterogeneous distributions (and magnetic properties) in post-annealed samples. These results are distinctly different from the average structure inferred by XRD which indicates distinct spinel phases only in the sample that is post-annealed at 1000°C. That is, FORC analysis appears sensitive to incipient demixing of the as-synthesized material at shorter length scales than probed by Bragg diffraction.

C. Average and local structure

The average and short-range order of these materials was further examined using neutron total scattering. Figure 7 illustrates the comparison of neutron diffraction and PDF data obtained at 300 K. Panel (a) compares the data from the higher resolution 154° 2θ detector bank (154° bank), where the presence of two spinel phases is indicated by clear peak splitting in the 1000°C sample data, while panel (b) compares the Bragg scattering data collected from the 31° 2θ detector bank (31° bank), including the peak that has both nuclear (111) and magnetic (101) contributions (d = 4.65 Å). The PDFs collected at 300 K for all four samples exhibit striking similarity over the first 10 Å, but the degree of similarity diminishes as the range expands (SI Figure S12).

Figure 7(c) provides a representative Rietveld refinement for the sample calcined at 400°C. The refinement method was extended to all data sets. Figure 8 illustrates the PDF refinement employing both 1-phase and 2-phase models below 30 Å. For improved comparative analysis, the low r range (from 1.7 Å to 6 Å) has been expanded. In the 1000°C sample data, where macroscopic phase segregation is evident at all length scales, a 2-phase model is significantly better than a 1-phase model. We found that a 2-phase model offers a significantly improved representation of the PDF in all samples in this study. This is overall consistent with results from STEM-EDS and FORC magnetometry- local nanoregions of chemically segregated but structurally similar spinel motifs are present in all samples. Since the regions have the same structural motif but different average chemistry, they feature slightly different lattice parameters. This leads to mostly overlapping PDF peaks at low real-space ranges and increasingly broadened PDF peaks at high real-space ranges in the PDF. A model allowing for two distinct lattice parameters and separately refined tetrahedral and octahedral site average scattering lengths captures the features of all PDFs well. Furthermore, as the post-annealing temperature increases to 800°C, the refinement quality improves and the discrepancies between the refinements obtained from 1-phase and 2-phase models diminish. This observation is consistent with our STEM-EDS results, which indicate that the post-annealing temperature contributes to greater spinel homogeneity. A summary of the Rietveld and

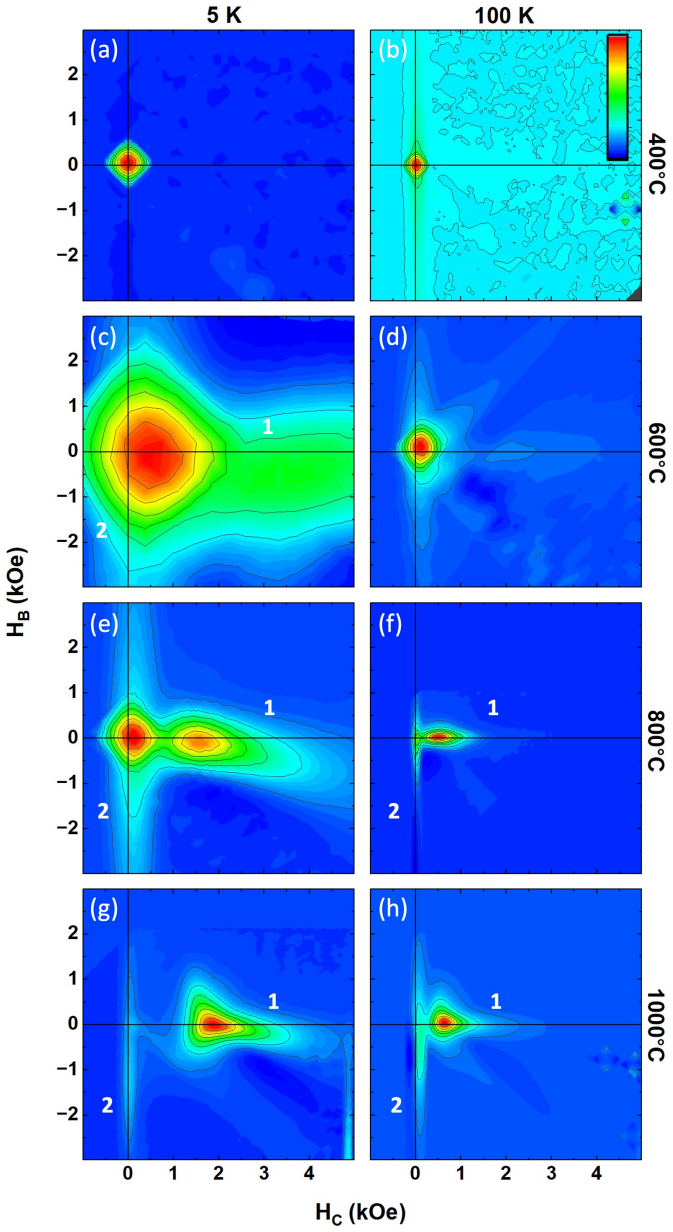

FIG. 6. The comparison of FORC measurements at 5 K and 100 K for the sample calcined at (a, b) 400°C and the samples post-annealed at (c, d) 600°C, (e, f) 800°C, and (g, h) 1000°C. The intensity scale for each panel, displayed at the top right of (b), is determined by its maximum (red) and minimum (blue) values. The feature labels "1" and "2" appearing in FORC plots for samples post-annealed at 600°C, 800°C, and 1000°C represent the primary feature orienting along the H_C axis, and the weak secondary feature along the H_B axis, respectively.

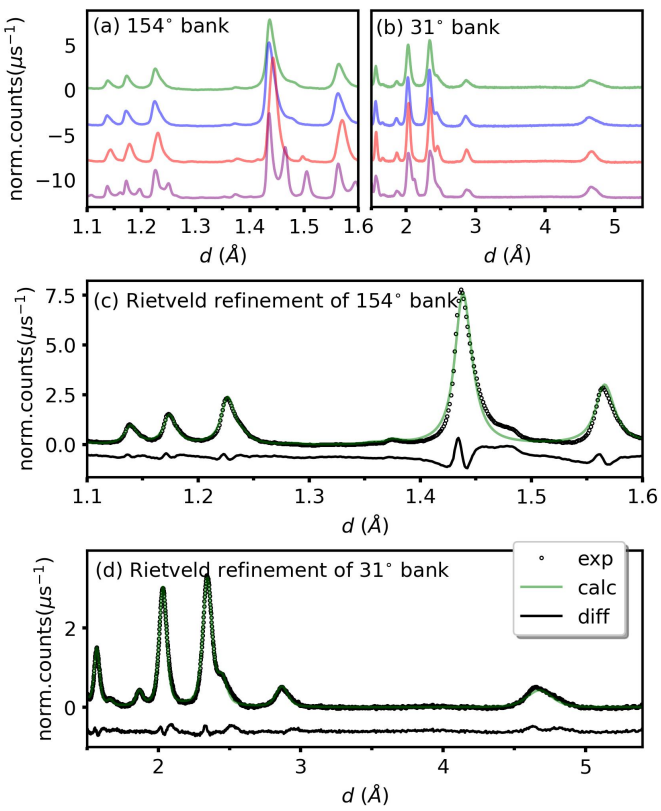

FIG. 7. The comparison of neutron diffraction data from the 154° 2θ detector bank (154° bank) (a) and 31° 2θ detector bank (31° bank) (b) for the samples that were calcined at 400°C (green), and post-annealed at 600°C (blue), 800°C (red), and 1000°C (purple). The fit results from the (c) 154° bank and (d) 31° bank for the Rietveld refinement of Bragg data (R_{wp}= 4.94%) pertain to the nanocrystalline CCO sample calcined at 400°C.

PDF refinement results is provided in SI Table S1. The key extracted parameters are summarized in Figure 9.

The Rietveld refinement analysis revealed that the phase percentage (p, %) of the main spinel remained near 100% across treatment conditions except in the sample post-annealed at 1000°C (Figure 9 (a)) which results in a secondary spinel phase. The lattice parameter (a, Å) of the main spinel trends slightly larger throughout the various heat treatments until the emergence of the secondary spinel at 1000°C (Figure 9 (b)). This secondary spinel has a larger lattice parameter than the main spinel phase. The average scattering lengths ($\langle b \rangle$, fm) refined for the tetrahedral and octahedral sites of the main spinel phase revealed a departure from random site ordering based on the average scattering length contributions of the composition (indicated with a solid black line, r-tet/oct). Neither do the refined site scattering lengths appear to correspond to inverse or normal site occupancy models. (The red dashed line and solid line indicate the calculated average scattering length on the tetrahedral site (n-tet) and octahedral site (n-oct) of a normal spinel structure, respectively. The red and black solid lines indicate the calculated average scattering length on the tetrahedral sites (i-tet) and octahedral sites (i-oct) with an inverse spinel configuration, respectively.) This in itself suggests a degree of chemical heterogeneity among all samples across the series (Figure 9 (c)). Finally, we note that because site occupancies are underdetermined in this Rietveld analysis, the presence or absence of cation vacancies cannot be disproved.

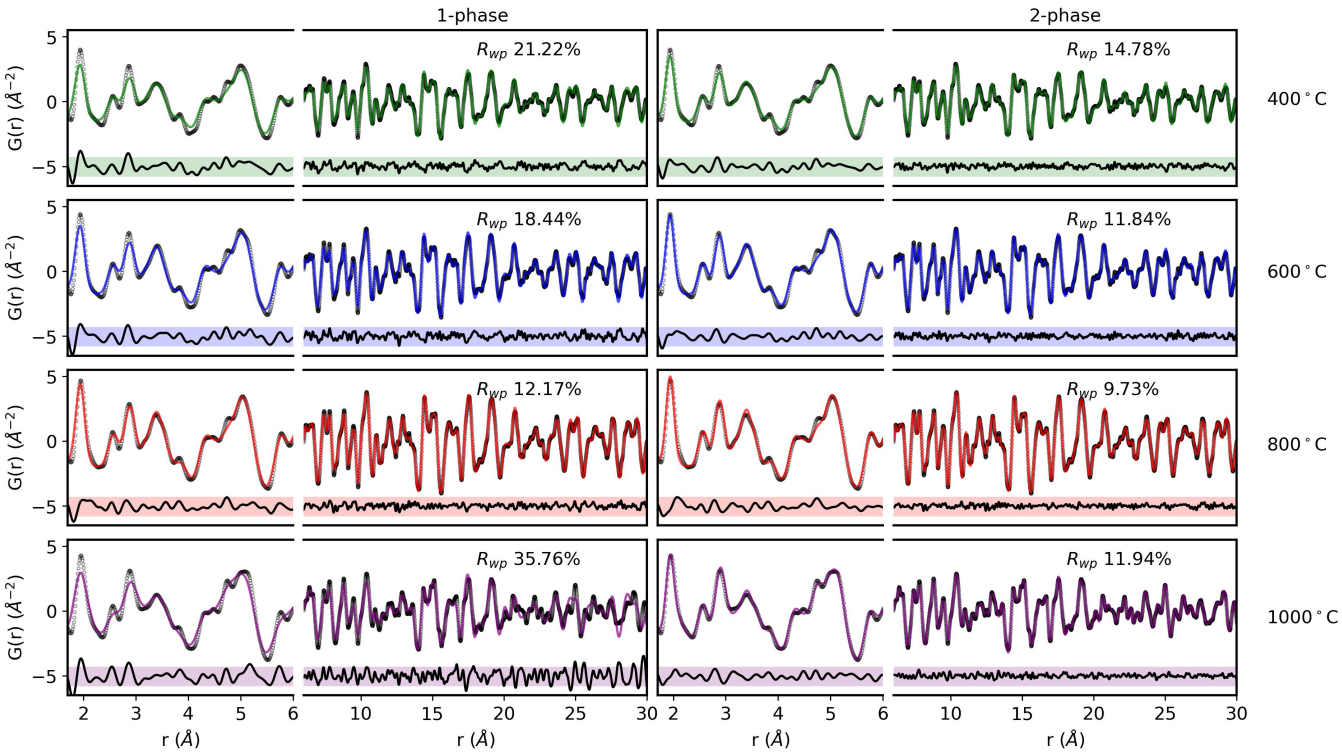

FIG. 8. Comparison of refinement results for the 30 Å PDF data range for samples that were calcined at 400°C, and post-annealed at 600°C, 800°C, and 1000°C, fit with a single spinel model (1-phase) on the left and a two-component spinel model (2-phase) on the right. Goodness of fit factors are displayed in each panel. For each panel, the low r range (from 1.7 Å to 6 Å) is expanded for enhanced comparison. Experimental data are illustrated by black circles, with the fits represented by colored lines. The black difference curves falling below the data and fits are highlighted in equally-sized green, blue, red, and purple boxes, calling attention to the different features corresponding to each specific sample.

Analysis of the PDF data over 30 Å yields further insight into the presence of distinct short range order (SRO) motifs in the samples. Structure refinement from PDF indicates the presence of a minor secondary spinel configuration at all sample treatment conditions (Figure 9 (d)). The analysis indicates that all samples feature local atomic configurations that resemble the long-range ordered 2-phase state present in the 1000°C sample. However, the amounts and metric expansion of the chemically distinct regions change slightly with post-annealing temperature (Figure 9 (d,e)) until the secondary spinel phase segregation is observed long-range in the sample post-annealed at 1000°C. The changes in refined $\langle b \rangle$s complement the inference of bulk diffusion and corresponding changes in CSRO obtained from STEM-EDS. In the secondary spinel phase model, $\langle b \rangle$s in the octahedral and tetrahedral sites are initially similar and larger than the values $\langle b \rangle$ in the main spinel phase. They shift to similar values in the sample post-annealed at 1000°C (Figure 9 (f)). In summary, PDF analysis indicates a continual rearrangement of cation site distribution leading at high post-annealing temperatures to long- range de-mixing and phase segregation. Additional Rietveld refinements were completed across the neutron diffraction data series using a similar 2-phase model (with phase fraction parameter and second cubic lattice parameter refined). Results are provided in SI Table S2, revealing a smaller secondary phase fraction and smaller difference in refined lattice parameters for the 800°C annealed sample data modeling. The results support conclusions made via PDF and STEM – the 800°C annealed sample has a more homogenous structure relative to other samples in the study.

Local rearrangement of the cation site distribution will influence the strength of ferrimagnetism in heterogeneous chemical regions, affecting bulk magnetism. Illustrative idealized examples of cation distribution in Figure 10(a-d) showcase two effects that may occur: the site inversion (γ) effect (a,b), and the phase segregation effect (c,d). Models in (c,d) are generated based on the STEM-EDS map of the sample post-annealed at 1000°C (Figure 3 (d)). A normal structure spinel structure was generated for $(Mg_{1/3}Cu_{1/3}Zn_{1/3})Co_2O_4$ in (c) since Mg and Zn are known to prefer the tetrahedral site and Cu demonstrates a partial preference, while an inverse spinel structure was generated for $(Co)(Mn_{0.5}Fe_{0.5}Co)O_4$ (d) due to the established preference of Mn^{2+} and Fe^{2+} for the octahedral site[44]. The corresponding calculated magnetic moments (μ_B) for the models are given in Figure 10 (e), and corresponding average scattering lengths $\langle b \rangle$ for the models are given in Figure 10 (f). Net moments were calculated assuming the maximum moment each cation can possess (Fe^{2+} 4.9 μ_B, Co^{3+} 4.9 μ_B, Cu^{2+} 1.73 μ_B, Mg^{2+} 0 μ_B, Zn^{2+} 0 μ_B, Mn^{2+} 5.92 μ_B)[45].

Overall, the calculated magnetic moments and average scattering lengths for the models in Figure 10 demonstrate that

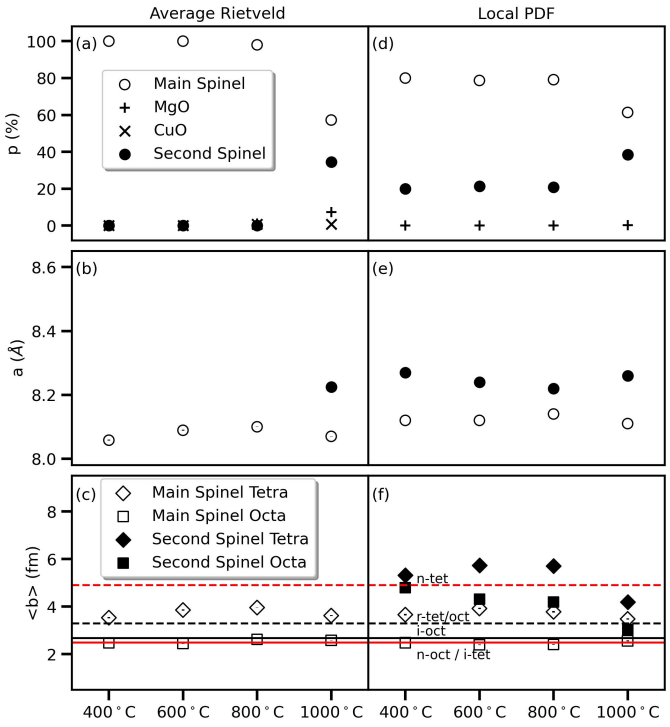

FIG. 9. Results of modeling neutron diffraction data (a, b, c) and PDF data (d, e, f) for the samples calcined at 400°C, and samples post-annealed at 600°C, 800°C, and 1000°C. (a, d) compares phase percentages (p, %), (b, e) compares lattice parameters (a, Å), and (c, f) compares average scattering lengths of tetrahedral and octahedral sites obtained from refinement ($\langle b \rangle$, fm). Note that the red dashed line and red solid line indicate the calculated average scattering length on the tetrahedral site (n-tet) and octahedral site (n-oct) of a normal spinel structure, respectively. The red solid line and black solid line indicate the calculated average scattering length on the tetrahedral site (i-tet) and octahedral site (i-oct) with an inverse spinel configuration, respectively. The black dashed line represents the calculated average scattering lengths on both tetrahedral and octahedral sites in a random spinel configuration (r-tet/oct).

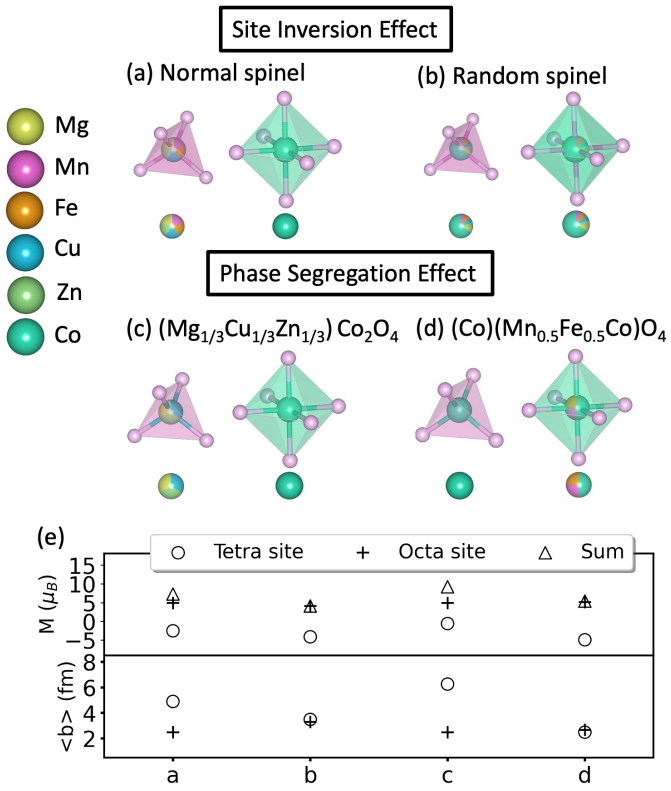

FIG. 10. Idealized illustrations of cation populations possible within a CCO spinel cobaltite, representing two observed effects: site inversion, represented by a possible (a) normal spinel, and (b) random spinel; and phase segregation, represented with (c) $(Mg_{1/3}Cu_{1/3}Zn_{1/3})Co_2O_4$, and (d) $(Co)(Mn_{0.5}Fe_{0.5}Co)O_4$. (e) Calculated magnetic moments (M) and average scattering lengths ($\langle b \rangle$, fm) for the models described in (a, b, c, d) on tetrahedral, and octahedral sites as well as the total sum of the magnetic moment.

variations can be realized through site inversion effects, phase segregation effects, and– by extension– combinations of multiple effects. While our PDF model cannot distinguish the specific effects occurring in our series, it is consistent with the observations of local chemical heterogeneity observed via STEM-EDS and hard/soft and coercive/reversible magnetic phases probed by FORC analysis.

Thus, FORC is diagnostic of the site inversion and local phase segregation effects occurring across the annealing series, corroborating the observation of two spinel phases in PDF local structure refinement in all samples and a precipitated second spinel phase in samples post-processed at 1000°C via Rietveld refinement.

IV. CONCLUSION

In summary, we have followed the magnetic properties, chemical segregation, and phase evolution of a nanostructured metastable compositionally complex spinel with chemical composition $(Mg_{0.2}Mn_{0.2}Fe_{0.2}Cu_{0.2}Zn_{0.2})Co_2O_4$, annealed at increasing post-processing temperatures.

A combination of FORC, STEM-EDS, and neutron total scattering analyses reveals that a two-step structure transformation occurs. Initially, the CCO synthesized by LTST at 400°C is a weak room-temperature ferrimagnet with cations distributed approximately at random across the tetrahedral and octahedral sites. In the first step, activated by post-processing at 600°C (supported by both FORC and neutron total scattering analysis), cations migrate locally among the tetrahedral and octahedral sites from a more random occupancy configuration to a more chemically specific arrangement. However, this localized transformation does not manifest as a medium or long-range effect in STEM-EDS mapping. In the second step, activated in samples annealed to 800 °C and above, long-range cation diffusion results in the demixing of the system into discrete segregated phases.

To understand the structure-property evolution in this series, the structural features at different length scales must be considered. STEM-EDS and neutron diffraction uncover long-range phase segregation of the sample post-annealed at 1000°C, but are insensitive to chemical short-range order present after synthesis. FORC analysis reveals the coexistence of soft and hard magnetic phases well before new bulk ordered phases emerge, consistent with neutron total scattering analysis. These findings emphasize the sensitivity of FORC analysis in identifying magnetic signatures as unique fingerprints of locally ordered structural domains.

The observation of rich complexity and structure-property tunability in a single CCO composition subjected to different post-processing temperatures highlights the great propensity and flexibility of CCOs as platforms in the design of complex functional oxides. In magnetic materials, one could design bulk hard-soft exchange spring magnets or exchange bias magnets through careful selection of the involved cations, the degree of local cation site mixing, and the propensity to form nano-segregated chemical short-range order in complex nanostructured phases.

Finally, this work reveals challenges in quantitatively capturing the crystal-chemical trends in a CCO featuring multiple cation sites, cation site inversion, and differing degrees of nanoscale chemical short-range order/phase segregation. The combined use of STEM-EDS, neutron diffraction/PDF, and FORC analyses only partially revealed the details of the detected multiple chemically segregated regions in the series. These findings underscore the need for combined characterization and analysis techniques when approaching complexity in CCOs. Further development of advanced characterization techniques for the broader crystal-chemical class of CCOs is warranted.

ACKNOWLEDGMENTS

XW, CSJ, CK, WM, DAG, and KP acknowledge the University of Tennessee - Oak Ridge Innovation Institute (UT-ORII) for Seed Funding supporting this work. Structural analysis of data is based upon work supported in part by the National Science Foundation under Grant DMR-2145174 (KP). This work used X-ray diffraction resources from the Diffraction Core Facility at the Institute for Advanced Materials and Manufacturing (IAMM) at the University of Tennessee. YPZ acknowledges the support from the US Department of Energy, Office of Science (contract No. DE-AC05-00OR22725). This research used BL-1B (NOMAD) at the Spallation Neutron Source, a DOE Office of Science User Facility operated by the Oak Ridge National Laboratory. The beam time was allocated at NOMAD on proposal number IPTS-29792.2.

DATA AVAILABILITY

The following file is available free of charge.

Supplemental Information: *Impact of thermal annealing on magnetic properties in nano compositionally complex spinel cobaltite - $(Mg_{0.2}Mn_{0.2}Fe_{0.2}Cu_{0.2}Zn_{0.2})Co_2O_4$*: The corresponding extracted phase percentages (p, %), lattice parameters (a, Å), average scattering lengths ($\langle b \rangle$, fm), and the atomic displacement parameters of tetrahedral cation, octahedral cation, and oxygen atom sites (B_{iso}, Å^2) of the PDF refinements conducted with ranges of 30 Å using both the 1-phase and 2-phase models are compared in Figure S1. Rietveld refinements for samples post-annealed at 800°C and 1000°C are illustrated in Figure S2. The STEM-EDS maps, along with their corresponding frequency histograms and a heatmap showing correlations between elemental pairs for each sample, are shown in Figures S3-S11. The PDF data comparison over 1.7 to 50 Å is shown in Figure S12. The summary of the Rietveld and PDF refinement results is provided in Table S1 and S2.

REFERENCES

[1] D. Pelc, R. J. Spieker, Z. Anderson, M. Krogstad, N. Biniskos, N. Bielinski, B. Yu, T. Sasagawa, L. Chauviere, P. Dosanjh, *et al.*, Unconventional short-range structural fluctuations in cuprate superconductors, Scientific reports **12**, 20483 (2022).

[2] J. Zhang, W.-J. Ji, J. Xu, X.-Y. Geng, J. Zhou, Z.-B. Gu, S.-H. Yao, and S.-T. Zhang, Giant positive magnetoresistance in half-metallic double-perovskite Sr_2CrWO_6 thin films, Science advances **3**, e1701473 (2017).

[3] Q. Zhang, Y. Zhang, M. Matsuda, V. O. Garlea, J. Yan, M. A. McGuire, D. A. Tennant, and S. Okamoto, Hidden local symmetry breaking in a kagome-lattice magnetic weyl semimetal, Journal of the American Chemical Society **144**, 14339 (2022).

[4] M.-Y. Yan, L.-H. Shu, Y. Xing, L.-D. Chen, X.-Y. Zhang, and S.-T. Zhang, Tailoring magnetic and dielectric properties of $Yb_2Ti_2O_7$ pyrochlore through structural distortion, Applied Physics Letters **121** (2022).

[5] B. Aktekin, F. Massel, M. Ahmadi, M. Valvo, M. Hahlin, W. Zipprich, F. Marzano, L. Duda, R. Younesi, K. Edstr om, *et al.*, How Mn/Ni ordering controls electrochemical performance in high-voltage spinel $LiNi_{0.44}Mn_{1.56}O_4$ with fixed oxygen content, ACS Applied Energy Materials **3**, 6001 (2020).

[6] A. R. Mazza, E. Skoropata, Y. Sharma, J. Lapano, T. W. Heitmann, B. L. Musico, V. Keppens, Z. Gai, J. W. Freeland, T. R. Charlton, *et al.*, Designing magnetism in high entropy oxides, Advanced Science **9**, 2200391 (2022).

[7] M. Harada, F. Kotegawa, and M. Kuwa, Structural changes of

spinel MCo_2O_4 (M= Mn,Fe,Co,Ni,andZn) electrocatalysts during the oxygen evolution reaction investigated by in situ x-ray absorption spectroscopy, ACS Applied Energy Materials **5**, 278 (2022).

[8] T. Roncal-Herrero, J. Harrington, A. Zeb, S. J. Milne, and A. P. Brown, Nanoscale compositional segregation and suppression of polar coupling in a relaxor ferroelectric, Acta Materialia **158**, 422 (2018).

[9] B. K. Khannanov, V. Zalessky, E. Golovenchits, V. Sanina, T. Smirnova, M. Shcheglov, V. Bokov, and S. Lushnikov, Separation of phases and charge states in relaxor ferroelectric $PbCo_{1/3}Nb_{2/3}O_3$, Journal of Experimental and Theoretical Physics **130**, 439 (2020).

[10] H. Xu, S. Jin, S. Lee, and P. E. Brown, Cation ordering, twinning, and pseudo-symmetry in silicate garnet: The study of a birefringent garnet with orthorhombic structure, American Mineralogist **108**, 572 (2023).

[11] N. A. Algarou, Y. Slimani, M. A. Almessiere, A. Baykal, S. Guner, A. Manikandan, and I. Ercan, Enhancement on the exchange coupling behavior of $SrCo_{0.02}Zr_{0.02}Fe_{11.96}O_{19}/MFe_2O_4$ (M= Co,Ni,Cu,MnandZn) as hard/soft magnetic nanocomposites, Journal of Magnetism and Magnetic Materials **499**, 166308 (2020).

[12] C. Xu, P. J. Reeves, Q. Jacquet, and C. P. Grey, Phase behavior during electrochemical cycling of Ni-rich cathode materials for Li-ion batteries, Advanced Energy Materials **11**, 2003404 (2021).

[13] Y. Shi, P. Jiang, S. Wang, W. Chen, B. Wei, X. Lu, G. Qian, W. H. Kan, H. Chen, W. Yin, *et al.*, Slight compositional variation-induced structural disorder-to-order transition enables fast Na^+ storage in layered transition metal oxides, Nature Communications **13**, 7888 (2022).

[14] P.-C. Wu, R. Huang, Y.-H. Hsieh, B. Wang, M. Yen, S.-Z. Ho, A. Kumamoto, C. Zhong, H. Song, Y.-C. Chen, *et al.*, Electrical polarization induced by atomically engineered compositional gradient in complex oxide solid solution, NPG Asia Materials **11**, 17 (2019).

[15] G. N. Kotsonis, S. S. Almishal, F. Marques dos Santos Vieira, V. H. Crespi, I. Dabo, C. M. Rost, and J.-P. Maria, High-entropy oxides: Harnessing crystalline disorder for emergent functionality, Journal of the American Ceramic Society **106**, 5587 (2023).

[16] X. Wang, P. Metz, E. Calì, P. R. Jothi, E. A. Lass, and K. Page, Phase selectivity and stability in compositionally complex nano $(nA_{1/n})Co_2O_4$, Chemistry of Materials **35**, 7283 (2023).

[17] J. Liang, J. Liu, H. Wang, Z. Li, G. Cao, Z. Zeng, S. liu, Y. Guo, M. Zeng, and L. Fu, Synthesis of ultrathin high-entropy oxides with phase controllability, Journal of the American Chemical Society (2024).

[18] J. Mohapatra, M. Xing, J. Elkins, and J. P. Liu, Hard and semihard magnetic materials based on cobalt and cobalt alloys, Journal of Alloys and Compounds **824**, 153874 (2020).

[19] W. Roth, The magnetic structure of Co_3O_4, Journal of Physics and Chemistry of Solids **25**, 1 (1964).

[20] C. Mariappan, R. Kumar, and G. V. Prakash, Functional properties of $ZnCo_2O_4$ nano-particles obtained by thermal decomposition of a solution of binary metal nitrates, RSC Advances **5**, 26843 (2015).

[21] S. Masoudpanah, Microwave absorption properties of $ZnCo_2O_4$ and $MnCo_2O_4$ powders synthesized by oxalate-assisted hydrothermal method, Journal of Materials Research and Technology **20**, 3750 (2022).

[22] Y. Bitla, Y.-Y. Chin, J.-C. Lin, C. N. Van, R. Liu, Y. Zhu, H.-J. Liu, Q. Zhan, H.-J. Lin, C.-T. Chen, *et al.*, Origin of metallic behavior in $NiCo_2O_4$ ferrimagnet, Scientific reports **5**, 15201 (2015).

[23] Y. Mouhib, M. Belaiche, S. Briche, C. A. Ferdi, and E. Iffer, Elaboration, characterization and first principle studies of $MnCo_2O_4$ nanomaterials prepared from non-standard raw materials, Materials Research Express **6**, 035508 (2018).

[24] S. Ali, H. Ullah, A. A. AlObaid, and T. I. Al-Muhimeed, Crystal field splitting, half metallic ferromagnetism, structural, mechanical and magneto-electronic properties of spinels type structure compounds MgX_2O_4 (X=FeandCo) for spintronic applications, The European Physical Journal Plus **136**, 1 (2021).

[25] R. Nakhowong and R. Chueachot, Synthesis and magnetic properties of copper cobaltite ($CuCo_2O_4$) fibers by electrospinning, Journal of Alloys and Compounds **715**, 390 (2017).

[26] A. Sarkar, R. Kruk, and H. Hahn, Magnetic properties of high entropy oxides, Dalton Transactions **50**, 1973 (2021).

[27] Q. Song and Z. J. Zhang, Shape control and associated magnetic properties of spinel cobalt ferrite nanocrystals, Journal of the American Chemical Society **126**, 6164 (2004).

[28] B. Musicó, Q. Wright, T. Z. Ward, A. Grutter, E. Arenholz, D. Gilbert, D. Mandrus, and V. Keppens, Tunable magnetic ordering through cation selection in entropic spinel oxides, Physical Review Materials **3**, 104416 (2019).

[29] L. Xu, C. Zhen, Z. Shui, D. Xu, L. Liu, L. Ma, D. Zhao, and D. Hou, Jahn-Taller distortion on exchange interactions between cations in $Mn_xCu_{1-x}Co_2O_4$ system, Journal of Physics D: Applied Physics **55**, 435003 (2022).

[30] X. Wang, B. L. Musicó, C. Kons, P. C. Metz, V. Keppens, D. A. Gilbert, Y. Zhang, and K. Page, Local cation order and ferrimagnetism in compositionally complex spinel ferrites, APL Materials **10** (2022).

[31] M. Brahlek, M. Gazda, V. Keppens, A. R. Mazza, S. J. McCormack, A. Mielewczyk-Gryń, B. Musico, K. Page, C. M. Rost, S. B. Sinnott, *et al.*, What is in a name: Defining "high entropy" oxides, APL Materials **10** (2022).

[32] X. Wang, H. Singh, M. Nath, K. Lagemann, and K. Page, Excellent bifunctional oxygen evolution and reduction electrocatalysts $(5A_{1/5})Co_2O_4$ and their tunability, ACS Materials Au **4**, 274–285 (2024).

[33] R. Taylor, Interpretation of the correlation coefficient: a basic review, Journal of diagnostic medical sonography **6**, 35 (1990).

[34] N. J. Gogtay and U. M. Thatte, Principles of correlation analysis, Journal of the Association of Physicians of India **65**, 78 (2017).

[35] D. A. Gilbert, G. T. Zimanyi, R. K. Dumas, M. Winklhofer, A. Gomez, N. Eibagi, J. Vicent, and K. Liu, Quantitative decoding of interactions in tunable nanomagnet arrays using first order reversal curves, Scientific Reports **4**, 4204 (2014).

[36] R. K. Dumas, C.-P. Li, I. V. Roshchin, I. K. Schuller, and K. Liu, Magnetic fingerprints of sub-100 nm Fe dots, Physical Review B **75**, 134405 (2007).

[37] C. R. Pike, A. P. Roberts, and K. L. Verosub, Characterizing interactions in fine magnetic particle systems using first order reversal curves, Journal of Applied Physics **85**, 6660 (1999).

[38] C. Pike, C. Ross, R. Scalettar, and G. Zimanyi, First-order reversal curve diagram analysis of a perpendicular nickel nanopillar array, Physical Review B **71**, 134407 (2005).

[39] A. P. Roberts, C. R. Pike, and K. L. Verosub, First-order reversal curve diagrams: A new tool for characterizing the magnetic properties of natural samples, Journal of Geophysical Research: Solid Earth **105**, 28461 (2000).

[40] J. Neuefeind, M. Feygenson, J. Carruth, R. Hoffmann, and K. K. Chipley, The nanoscale ordered materials diffractometer NOMAD at the spallation neutron source SNS, Nuclear In-

struments and Methods in Physics Research Section B: Beam Interactions with Materials and Atoms **287**, 68 (2012).

[41] A. A. Coelho, TOPAS and topas-academic: an optimization program integrating computer algebra and crystallographic objects written in C^{++}, Journal of Applied Crystallography **51**, 210 (2018).

[42] A. C. Larson and R. B. Von Dreele, Gsas, Report lAUR , 86 (1994).

[43] Y. Zhang, J. Liu, and M. G. Tucker, Lorentz factor for time-of-flight neutron bragg and total scattering, Acta Crystallographica Section A: Foundations and Advances **79** (2023).

[44] R. W. Grimes, A. B. Anderson, and A. H. Heuer, Predictions of cation distributions in AB_2O_4 spinels from normalized ion energies, Journal of the American Chemical Society **111**, 1 (1989).

[45] S. Mugiraneza and A. M. Hallas, Tutorial: a beginner's guide to interpreting magnetic susceptibility data with the curie-weiss law, Communications Physics **5**, 95 (2022).